Acta Materialia 242 (2023) 118456

Contents lists available at ScienceDirect

Acta Materialia

journal homepage: www.elsevier.com/locate/actamat

# Effect of volume fractions of gradient transition layer on mechanical behaviors of nanotwinned Cu

Zhao Cheng[a,1], Tao Wan[a,b,1], Linfeng Bu[a,c], Lei Lu[a,*]

[a] Shenyang National Laboratory for Materials Science, Institute of Metal Research, Chinese Academy of Sciences, Shenyang 110016, China
[b] School of Materials Science and Engineering, University of Science and Technology of China, Shenyang 110016, China
[c] CAS Key Laboratory of Mechanical Behavior and Design of Materials, Department of Modern Mechanics, CAS Center for Excellence in Complex System Mechanics, University of Science and Technology of China, Hefei 230027, China

ARTICLE INFO

*Article history:*
Received 16 August 2022
Revised 17 October 2022
Accepted 20 October 2022
Available online 23 October 2022

*Keywords:*
Heterogeneous nanostructured metals
Gradient transition layer
Strengthening behavior
Distribution of GNDs
Back stress

ABSTRACT

Heterogeneous nanostructured (HNS) materials, such as gradient and laminated nanostructured metals, possess superior mechanical properties with respect to their homogeneous counterparts. The additional strengthening mechanism of HNS is mainly attributed to the non-uniform plastic deformation induced by gradient transition layers (GTLs) between components. Here, we designed three gradient nanotwinned (GNT) Cu samples with different volume fractions of GTLs ($f_g$) of 10%, 50% and 100% while the rule-of-mixture strength and overall structural gradient are constant to quantitatively reveal its effect on the extra strengthening behaviors. As $f_g$ increases, the yield strength is improved and the elastic to plastic stage is prolonged at small strain. Moreover, larger $f_g$ suppresses the strain localization and reduces nucleation of cracks at larger strain, accompanied by more widely distributed geometrically necessary dislocations (GNDs) and more bundles of concentrated dislocations (BCDs), thus improving the elongation. Stress partitioning analysis and numerical simulations show that the more widely-distributed GNDs at larger $f_g$ result in higher overall back stresses but hardly affect effective stresses, indicative of the origin of the improved strengthening. Such GND-distribution dominated strengthening mechanism paves a fundamental way for developing higher-performance HNS materials.



## 1. Introduction

Hetero-structured materials are defined as materials that contain heterogeneous regions that exist between constituent components with different mechanical properties [1,2]. Experiments and modeling investigations [3–7] have demonstrated that hetero-structured materials benefit from the synergistic effect arising from the interaction and coupling between these heterogeneous zones, particularly when at least one of characteristic length scales is reduced to the nanoscale, as in the case of heterogeneous nanostructured (HNS) metals.

As a typical HNS materials, the laminated metals with interfaces or sharp gradient transition layers (GTLs) between components generally exhibit good strength-ductility synergy [8–12]. The underlying strengthening mechanism of laminated structure is closely related to the interface-coordinated deformation that strain gradient and geometrically necessary dislocations (GNDs) are accumulated intensively at interfaces, where an interface affected zone forms with tens of micrometers in width [8,13]. The mechanical properties of laminated structure are sensitive to the interface spacing, i.e., the smaller interface spacing or more interface affected zone induces the higher overall GND density, yielding a higher strength.

Unlike the sharp interface (or GTL) in laminated structure, gradient structures typically have wider GTLs where the characteristic sizes of the microstructure (grain size or/and twin thickness, etc.) vary successively and progressively from the nanoscale to hundreds or thousands of micrometers within the macroscopic thickness of the samples [3,14-16]. For example, surface mechanical treatment procedures, including surface mechanical grinding treatment [14], surface mechanical attrition treatment [15], friction sliding deformation [17], etc., have been well-developed to introduce surface gradient nanograined structure in various metallic materials. Although the GTLs introduced by surface fabrication methods are commonly located only on the sample surfaces with an average depth of several hundred micrometers and a total volume fraction of 20%~25% [3,14,16], gradient nanograined materials also exhibit good strength-ductility, compared to their homogeneous components.

* Corresponding author.
*E-mail address:* llu@imr.ac.cn (L. Lu).
[1] These authors contributed equally to this work.

https://doi.org/10.1016/j.actamat.2022.118456
1359-6454/

Gradient nanotwinned (GNT) Cu with dual-gradient of both grain size and twin thickness has been fabricated by means of electrodeposition technique [4,18,19]. In this case, the GTL spans the entire thickness of the sample with a volume fraction up to 100%. It was found that the strength and work hardening of GNT Cu surpass the corresponding rule-of-mixtures estimates from their homogeneous components, and they monotonously increase with increasing structural gradient, showing a significant extra strengthening. Here the structural gradient, defined as the hardness variation per unit distance along the gradient direction, can be accurately tuned by controllable patterning of homogeneous nanotwinned (HNT) components from monotonic, symmetric periodic to multi-periodic spatial variations. When the structural gradient is sufficiently large, the strength of GNT Cu even exceeds the upper limit of the strongest component. By comparing to the postmortem microstructure of HNT components, it was revealed that numerous bundles of concentrated dislocations (BCDs) are the dominant dislocation patterns, which are dispersedly distributed, coinciding with the direction of structural gradient and perpendicular to TBs. This typical BCD structure as GND configuration and running through almost the entire length of part of grains causes an increase of plastic strain gradient and contributes to extra back stresses [19].

Overall, the strengthening mechanisms of HNS materials are closely related to the interaction and coupling of the non-uniform plastic deformation at their GTLs [7,20-22]. Accompanying with the orderly progressive yielding among components with different yield strengths (or at different length scales), GNDs are generated as a geometrical requirement of the plastic strain gradient [23–25]. Most importantly, additional GNDs provide not only kinematic strengthening but also strain hardening [26–28], thus contribute to both strength and ductility. The relationship between the density (or type) of GND and flow stress/strength has been extensively studied over the last few decades [6,7,24,29-31]. Increasing the density of GND through smaller interfacial spacing or larger structural gradients can stimulate stronger strengthening effect of HNS materials [4,8]. In fact, gradient plastic deformation and the resulting GND distribution are not identical for HNS materials with different structures, as they have different GTL distributions, such as the aforementioned sharp interface affect zone [8], gradient nanograined layers [14] and full gradient GNT structures [4]. Unfortunately, quantitative studies on the effects of GND distribution on the deformation behavior and strengthening mechanisms of HNS are still lacking so far.

In this study, we designed/adjusted the distribution of GNDs by changing the volume fraction of GTL ($f_g$) to quantitatively explore the mechanical behaviors of different HNS materials. Three GNT Cu samples with different $f_g$ ranging from near zero (laminated) to 100% (fully spatial gradient), while the rule-of-mixture strength and overall structural gradient keep constant, were designed and fabricated. Combining uniaxial tensile tests, full-field strain mapping and systemically microstructure characterization, the effect of $f_g$ on the tensile properties, the spatial distribution of gradient plastic strains and GNDs (or BCDs) are systematically studied in GNT Cu samples. Stress partitioning and numerical simulation were also used to further analyze the strengthening kinematics related to the distribution of GNDs and back stresses.

## 2. Experimental and modeling methods

### 2.1. Sample preparation

In this study, only two HNT components, namely hard Ⓐ and soft Ⓓ [4], are used to design three types of representative HNS materials with different volume fractions of GTLs, like the sandwich structures with hard surfaces and soft core shown in Fig. 1a1-c1. First is a laminated structure with sharp interfaces between hard surfaces Ⓐ and soft core Ⓓ (Fig. 1a), i.e., $f_g$ is near zero (∼10% resulting from fluctuated interfaces in the as-prepared sample). Third is a fully continuous gradient sample from hard Ⓐ to soft Ⓓ, i.e., $f_g$ =100% (Fig. 1c). In between, a sample with $f_g$ =50% is designed as well, where the GTLs are located between Ⓐ and Ⓓ (Fig. 1b). For clarity of discussion, we named the three samples as GNT-10%, GNT-50% and GNT-100% based on its $f_g$. Regarding three GNT Cu samples, the average strength from rule of mixture and the overall structural gradient across the whole samples are the same.

Firstly, two HNT Cu are prepared by means of direct-current electrodeposition at 20 and 40 °C, respectively, which are referred to as the freestanding hard Ⓐ and soft Ⓓ components. The current density and the total deposition time are fixed as 30 mA/cm$^2$ and 16 h, yielding a constant sample thickness of ∼400 $\mu$m. Three GNT Cu samples were prepared through carefully adjusting the electrolyte temperatures. The GTLs in GNT Cu samples are deposited by linearly increasing the temperature from 20 to 40 °C or decreasing temperature from 40 to 20 °C. The deposition time for each GTL in GNT-10%, GNT-50% and GNT-100% were set from 0.1, 4 and 8 h, respectively, and that means the thickness of each GTL is ∼20, 100 and 200 $\mu$m, respectively. More details for the electrodeposition setups can be found elsewhere [4].

### 2.2. Microstructure characterization

The cross-sectional microstructures of as-deposited three GNT Cu samples were examined by scanning electron microscope (SEM) FEI Verios 460 using backscattering electron (BSE) imaging mode and transmission electron microscope (TEM) FEI Tecnai G2 F20 TEM with accelerated voltage of 200 kV. The average grain size and twin thickness of each component were obtained from more than 500 grains in SEM images and more than 1000 twin lamellae in TEM images with edge-on twin boundaries (TBs), respectively. The preparation of SEM and TEM specimens can be found in [4].

The microstructures of deformed GNT Cu samples are also observed by SEM and TEM. The frequency of grains with BCDs at a component was obtained by examining over 200 grains in SEM images. A dual-beam diffraction technique in TEM under a diffraction vector of $\boldsymbol{g} = 200$ was used to further detect detailed dislocation types of BCDs.

The Kernel average misorientation (KAM) for deformed GNT Cu were also measured by electron backscatter diffraction (EBSD) with a step size of 100 nm in the SEM FEI Nova NanoSEM 450 under a voltage of 20 kV. Oxford HKL channel 5 software was used to analyze the obtained data. The misorientation of each point was calculated using the KAM method with 3 × 3 filter size where the local misorientation larger than 3° was regarded to be induced by the grain boundary and was excluded. Local dislocation density was calculated through $\rho = 2\theta/lb$ [13], where $\theta$ is the local misorientation, $l$ is the unit length (100 nm) and $b$ is the Burgers vector of Cu (0.255 nm)

The cross-sectional hardness distribution of GNT Cu was measured using a Qness Q10A+ micro-hardness tester with a load of 50 g and dwelling time of 10 s. Five individual indents were measured to get the average hardness at a given depth.

### 2.3. Uniaxial and loading-unloading-reloading tensile tests

Uniaxial tensile tests of three GNT Cu specimens with a 5-mm gage length and a 1.5-mm width of were performed on an Instron 5848 microtester at ambient temperature. The tensile strain of the gage section is monitored by means of an MTS LX300 laser extensometer. The strain rate is 5 × 10$^{-3}$ s$^{-1}$ for all tensile texts. As for each GNT Cu sample, at least 4 specimens were tested to ensure the repeatability.

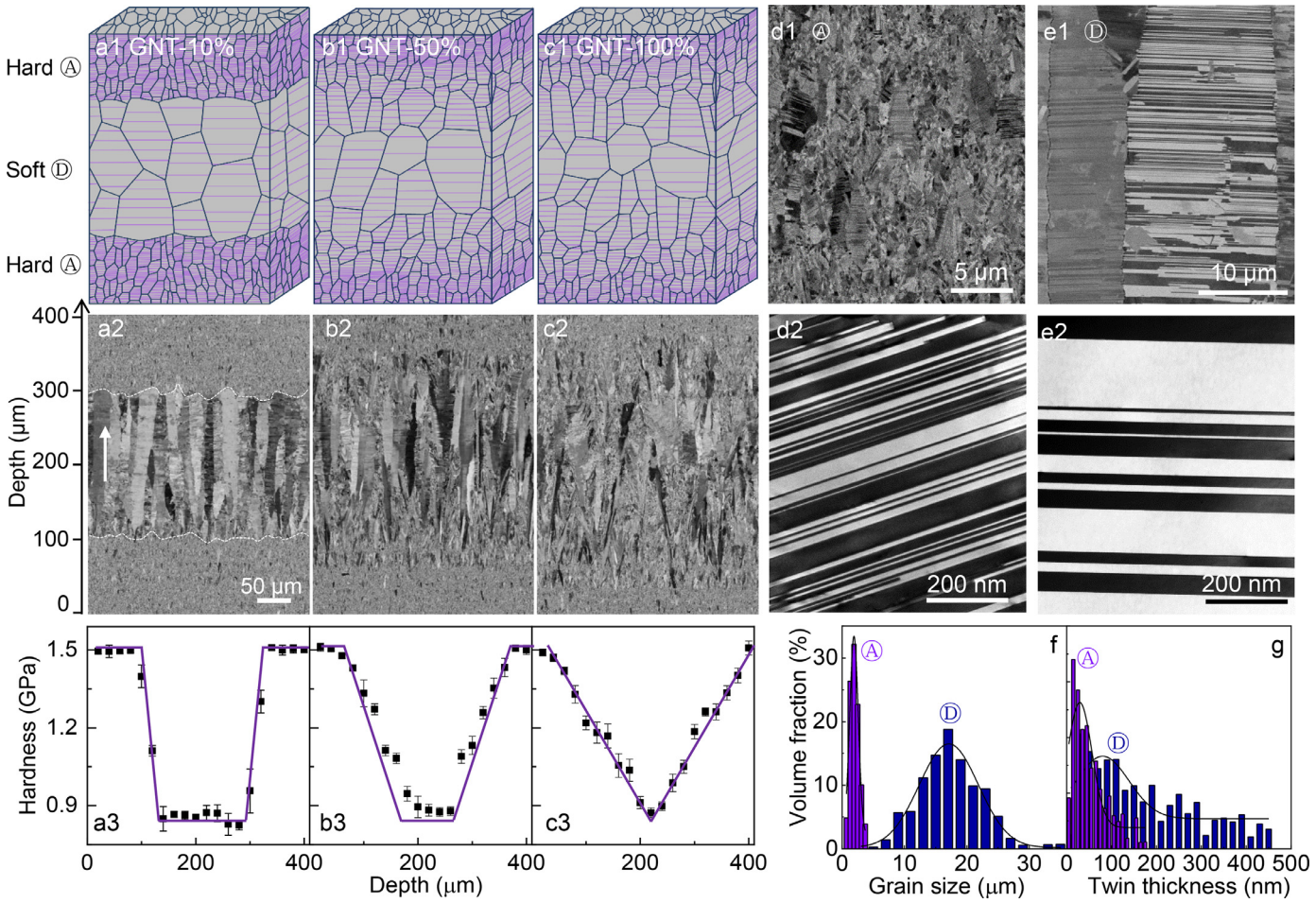


**Fig. 1.** The schematics, cross-sectional SEM image and hardness distribution of GNT-10% (a1-a3), GNT-50% (b1-b3) and GNT-100% (c1-c3). The SEM and TEM images of hard component Ⓐ (d1, d2) and soft component Ⓓ (e1, e2). The distributions of grain size (f) and twin thickness (g) of Ⓐ and Ⓓ. The white arrow in (a2) represents the growth direction of GNT Cu samples by electrodeposition .

The loading-unloading-reloading process was conducted on Instron 5848 microtester with a contactless strain gaging system based on digital image correlation technique to detect the evolution of back stress and effective stress [32]. The loading or reloading was controlled using the crossover displacement of the microtester at a strain rate of $1 \times 10^{-3}$ $s^{-1}$. The unloading was controlled by the load force at a rate of 70 N/min and the limit of unloading is set by 10 N. Based on the classical Dickson's method [33,34], the back stress $\sigma_b$ and effective stress $\sigma_{eff}$ can be calculated by

$$\sigma_b = \frac{\sigma_f + \sigma_{ry}}{2} - \frac{\sigma^*}{2} \tag{1}$$

$$\sigma_{eff} = \sigma_f - \sigma_b \tag{2}$$

where $\sigma_f$ is the true flow stress at unloading point, $\sigma_{ry}$ is the reverse yield stress upon unloading and $\sigma^*$ is the stress interval past the peak stress. $\sigma_{ry}$ is determined by the reference elastic unloading curve with a slope of elastic modulus $E$ (~120 GPa for Cu) and an offset strain $\delta$ intercepting the unloading curve, as schematically shown in Fig. 6(b). $\delta$ was chosen as 0.01% which should be small enough to satisfy the assumption that the back stress is constant during the elastic unloading.

### 2.4. Strain mapping and fracture observation

An in-situ full-filed strain technique based on digital image correlation was used to characterize the local strain distributions on the top and lateral surfaces of GNT Cu samples. Before digital image correlation observations, the spackle black ink pattern on the top surfaces of the samples was sprayed on a painting white background. The digital image correlation observations were conducted using an optic lens with a magnification of 2. The strain distribution mapping was analyzed using VIC-2D system with a resolution of 2.9 $\mu$m/pixel on top surface and 0.5 $\mu$m/pixel on lateral surface.

The deformed microstructure near the fracture was examined in SEM by using the BSE imaging mode. The fracture surfaces were observed using a LEICA-DMRX optical microscope (OM) under dark field mode.

### 2.5. Numerical simulations

A one-dimensional strain gradient plasticity model was developed to further explore the tensile responses such as overall flow stress and spatial distribution of strain/stress to different $f_g$ in GNT Cu. The model is formulated based on the $J_2$ flow theory. The constitutive equations and numerical details are presented in [19]. The total flow stress is decomposed into three parts, i.e., effective stress, HNT-induced back stress and extra back stress arising from structural gradient

$$\sigma_f = \sigma_{eff} + \sigma_b^{HNT} + \sigma_b^{GNT} \tag{3}$$

The effective stress$\sigma_{eff}$ is assumed to arise from the conventional Taylor hardening and depends mainly on the dislocation density. The HNT induced back stress $\sigma_b^{HNT}$ originates from the incom-

**Table 1**
Tensile properties of GNT Cu samples and Ⓐ and Ⓓ components. $\sigma_y$, yield strength; $\sigma_{1\%}$ and $\sigma_{4\%}$ are flow stresses at $\varepsilon_{app}$=2% and 4%, respectively; $\sigma_{uts}$, ultimate tensile strength; $\delta_u$, uniform elongation; $\delta_f$, elongation to failure; $\varepsilon_{e\text{-}p}$, the ending strain of elastic to plastic stage.

| Sample | $\sigma_y$ (MPa) | $\sigma_{1\%}$ (MPa) | $\sigma_{4\%}$ (MPa) | $\sigma_{uts}$ (MPa) | $\delta_u$ (%) | $\delta_f$ (%) | $\varepsilon_{e\text{-}p}$ (%) |
|---|---|---|---|---|---|---|---|
| GNT-10% | 337±8 | 384±6 | 402±5 | 404±5 | 7.7 ± 0.4 | 15.4 ± 2.5 | 1.5 |
| GNT-50% | 347±13 | 391±6 | 408±2 | 410±2 | 7.3 ± 0.3 | 16.0 ± 1.2 | 1.7 |
| GNT-100% | 373±7 | 399±2 | 417±4 | 419±3 | 7.4 ± 0.5 | 18.3 ± 2.2 | 1.9 |
| Hard Ⓐ | 434±9 | | | 501±14 | 1.6 ± 0.1 | 15.3 ± 2.5 | 1.3 |
| Soft Ⓓ | 188±3 | | | 280±2 | 25.1 ± 1.1 | 34.6 ± 2.5 | 2.4 |

patible deformation across twin boundaries and is inversely proportional to twin thickness. The structural gradient induced back stress $\sigma_b^{GNT}$ stems from GNDs for accommodating the strain gradient across the built-in gradient structures of GNT Cu and is proportional to GND density and GND characteristic length.

In the previous study [19], the contribution of GND density for the back stress was focused on to unravel the effect of structural gradient but the physics of GND characteristic length was less discussed. In the modeling, we further modified the strain gradient plasticity model by linking the GND characteristic length with the GND distribution when the overall GND density or structural gradient is constant for GNT Cu samples with different $f_g$, just as the design in the experimental. Note that the gradient deformation is assumed to only exist in the GTL based on the experimental results (Fig. 4f).

## 3. Results and discussion

### 3.1. Microstructure characterization of GNT Cu samples

The microstructures of the two HNT components (hard Ⓐ and soft Ⓓ) are characterized firstly by means of SEM and TEM techniques, as shown in Fig. 1d1-e2. Both components possess highly oriented nanotwinned structures that multiple nanoscale twin lamellae perpendicular to the growth direction are embedded in micron-scale columnar grains. The average grain size (Fig. 1f) and twin thickness (Fig. 1g) of hard Ⓐ are 1.9 $\mu$m and 29 nm, respectively, obviously smaller than those (17.1 $\mu$m and 80 nm) of soft Ⓓ.

As expected, SEM images in Fig. 1a2-c2 show the cross-sectional observations of microstructure of GNT-10%, GNT-50% and GNT-100% with different $f_g$. GNT-10% shows a sandwiched structure separated by two sharp and curved interfaces, as outlined in Fig. 1a2. The fluctuations of up and lower interfaces are ~25 and ~15 $\mu$m along the growth direction, respectively, forming into two GTLs with volume fraction of 10%. The hardness jumps from 1.5 GPa of surface hard Ⓐ into 0.8 GPa in the core soft Ⓓ. Different from GNT-10%, Ⓐ with a thickness of about 50 $\mu$m are located in the two top surfaces and Ⓓ with a thickness of 100 $\mu$m are located in the core in GNT-50% (Fig. 1b1 and b2). In between, there are two GTLs from Ⓐ to Ⓓ with linearly changed hardness (Fig. 1b3). Each one spans 100 $\mu$m and both GTLs account 50% for the total volume (or sample thickness), so it is named as GNT-50%. GNT-100% has a 100% gradient microstructure (Fig. 1c2) and linearly increased hardness from core to surface (Fig. 1c3). Both rule-of-mixture hardness (~1.15 GPa) and the overall structural gradient (~3.5 GPa/mm) are the same for three GNT Cu.

### 3.2. Mechanical properties of GNT Cu samples

Fig. 2a shows the tensile engineering stress-strain curves of three GNT Cu samples with two freestanding HNT components for comparison. The freestanding Ⓐ has a high yield strength (434 MPa) and a limited uniform elongation (1.6%), while Ⓓ exhibits a lower yield strength (186 MPa) and larger uniform elongation (24.8%), as shown in Table 1.

From GNT-10% to GNT-100%, the yield strength increases from 337 MPa up to 373 MPa, much higher than the rule-of-mixture strength (310 MPa). In terms of ductility, the uniform elongation upon necking keeps around 7.5%, but the elongation to failure increases slightly from 15.4% to 18.3% from GNT-10% to GNT-100%. Above results suggest a higher extra strengthening and a better strength-ductility synergy can be achieved by tuning $f_g$ from 10% to 100% in GNT Cu.

Fig. 2b shows the work hardening rates versus true strain of three GNT Cu samples. Two typical stages are observed in three GNT Cu samples. The first is the elastic-to-plastic stage where work hardening rate decreases rapidly at small strains. The ending strain of this stage, $\varepsilon_{e\text{-}p}$, is defined as the strain for the work hardening rate reducing down to $E$/100 [35,36]. Another is the steady plastic deformation stage where work hardening reduces slowly at larger strains. For GNT-10% to GNT-100%, the work hardening rate in the elastic-to-plastic stage markedly increases and $\varepsilon_{e\text{-}p}$ from 1.5% to 1.9%, between hard Ⓐ and soft Ⓓ (Table 1). Such prolonged elastic-to-plastic stage is consistent with the improvement of the yield strength. Whereas three GNT Cu samples exhibit comparable work hardening rate at steady stage. That means, the extra strengthening contributed by $f_g$ mainly happens in the initial elastic to plastic stage.

### 3.3. Characterization of plastic strain evolution of GNT Cu samples

The distribution of lateral strain ($\varepsilon_z$) along the sample thickness on the lateral surface ($x$-$z$ plane, colored by red in Fig. 3a) of GNT Cu samples to characterize the gradient deformation is measured by in-situ digital image correlation. As for GNT-10% at an applied strain $\varepsilon_{app}$=0.5% (Fig. 3b1), the magnitude of $|\varepsilon_z|$ is larger in the core than that at surface. Such strain discrepancy is related to the strength gradient across components Ⓐ and Ⓓ. The soft Ⓓ with lower yield strength sustains a larger tensile plastic strain. Since the Poisson's ratio for lateral strains is larger at the plastic deformation than at the elastic [37], Ⓓ exhibits a larger $|\varepsilon_z|$. Notably, $|\varepsilon_z|$ jumps steeply across the sharp interfaces, suggesting where a concentrated strain gradient or deformation incompatibility happens. As $\varepsilon_{app}$ increases, $|\varepsilon_z|$ increases but the strain gradient still localizes intensively at interfaces (Fig. 3b2 and 3b3). However, compared to GNT-10%, the lateral strain gradually and continuously increases from core to surface in GNT-100% (Fig. 3c1-c3), where the strain gradient is more uniformly distributed throughout the whole sample without any severe concentrations.

Intrinsically, the strain gradient reflects on GNDs assisted deformation according to the classic theory of strain gradient plasticity [23–25]. The distributions of GNDs on the cross-section ($x$-$z$ plane, the same as that in Fig. 3a) of GNT Cu deformed at $\varepsilon_{app}$=1% were detected by combining SEM, EBSD and TEM observations (Figs. 4 and 5). Regarding GNT-10%, SEM images in Fig. 4a-c show both hard Ⓐ and soft Ⓓ still keep the typical columnar grains with nanotwins and the well bonded sharp interfaces still retains. No

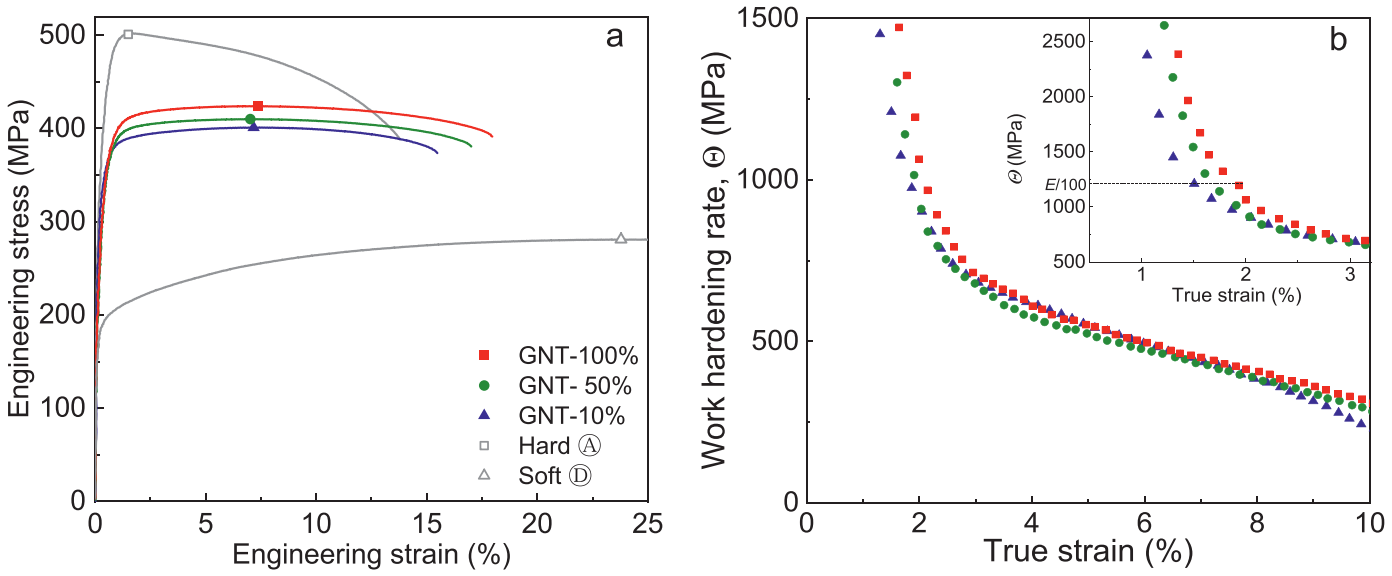


**Fig. 2.** (a) The engineering tensile stress-strain curves of GNT-10%, GNT-50% and GNT-100% and their freestanding Ⓐ and Ⓓ components. (b) Work hardening rate-true strain curves of GNT-10%, GNT-50% and GNT-100%. The inset of (b) shows the magnified work hardening curves at small strains. The work hardening rate $\Theta=E/100$ ($E$, elastic modulus) indicated by dash line was used to identify the ending of elastic to plastic stage.

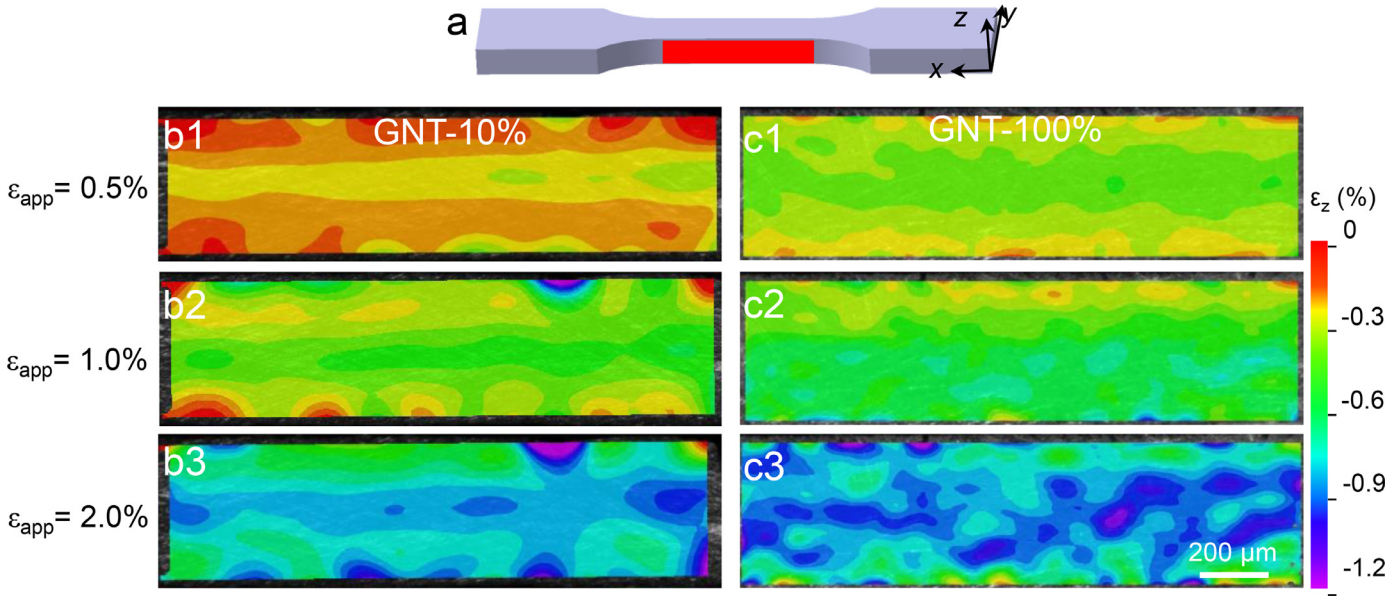


**Fig. 3.** (a) The schematics illustrating the strain distribution measurement on the lateral surface ($x$-$z$ plane) indicated by red in GNT Cu. The distribution of lateral strain $\varepsilon_z$ of GNT-10% (b1-b3) and GNT-100% (c1-c3) at increasing applied tensile strain $\varepsilon_{app}$ as indicated.

visible dislocation structure is detected in interiors of either Ⓐ or Ⓓ or at interfaces. From the EBSD mapping in the region crossing the interface (Fig. 4d), soft Ⓓ exhibits a strong {111} texture while hard Ⓐ shows a weaker texture, suggesting an obvious microstructure difference between both sides of the interface. The dislocation distribution is obtained based on the EBSD mapping in Fig. 4e. Obviously, the average dislocation density shows a peak around the interface and decreases along the direction away from the interfaces (Fig. 4f). The dislocation peak has a width of ~10 $\mu$m, which is consistent with the size of interface affected zone with accumulated GNDs in other laminated materials without nanotwins [8]. The GNDs storage at interfaces is also consistent with the concentrated strain gradient in Fig. 3b1-b3.

GNT-100% at $\varepsilon_{app}$=1% exhibits a distinct deformation morphology that several long BCDs appear with strong contrast (indicated by red arrows) along the gradient direction, as shown in the across-sectional SEM image in Fig. 5a. The orientation distribution of Fig. 5a is further analyzed by EBSD in Fig. 5b. GNT-100% exhibits strong {111} texture throughout the sample. The orientation varies obviously across BCDs (indicated by white arrows in Fig. 5b). Statistic results suggest that BCDs have various misorientations ($\theta$) from 6 to 8° and span the widths ($l$) of 1.5~4 $\mu$m at three different positions (marked by 1, 2 and 3) as shown in Fig. 5c. The density of GND ($\rho_{GND}$) in BCD is estimated to be about ~$10^{14}$ $m^{-2}$ by $\rho_{GND}=\theta/lb$ where $b$ is the dislocation Burgers vector (0.255 nm). Both the morphology and the density of GNDs of GNT-100% are similar to that in four-component GNT Cu in [4,19].

The details of BCDs were further characterized by low-magnification TEM in Fig. 5d, which shows a long BCD spanning multiple twin lamellae. Inside the BCD, a few Mode I dislocation [38] fragments with both glide plane and glide direction inclined to TBs are observed. The dual-beam diffraction technique in TEM [38] was used to identify the dislocation components of BCD, as shown in Fig. 5e where TBs are tilted away from the edge-on un-

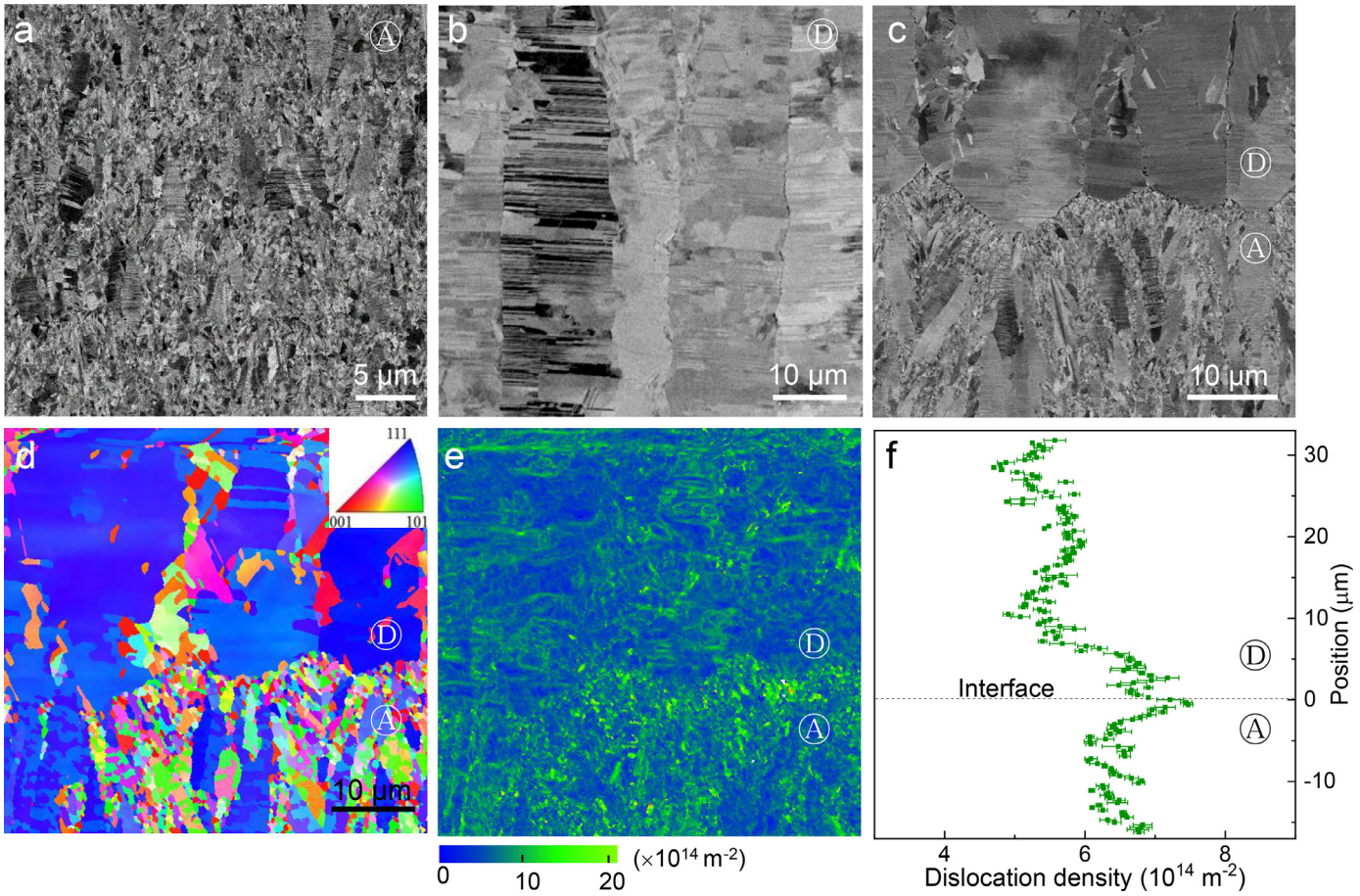


**Fig. 4.** Cross-sectional (*x-z* plane) microstructure of GNT-10% deformed at $\varepsilon_{app}$=1%. SEM images of hard Ⓐ (a), soft Ⓓ (b) and the region across interface (c) of GNT-10% at $\varepsilon_{app}$=1%. EBSD orientation mapping (d), dislocation density mapping (e) and corresponding average dislocation density distribution (f) of the region across interface at $\varepsilon_{app}$=1%, respectively.

der the diffraction vector $\boldsymbol{g}$ = 200. Many dislocation fragments at TBs are identified as Mode II dislocations [38], whose glide plane and direction is inclined and parallel to TBs, respectively. The density of Mode II dislocation reaches ~$10^{14}$ $m^{-2}$, which is about two orders of magnitude higher than that of Mode I. In other words, BCDs are composed of numerous Mode II and few Mode I dislocations. Parts of Mode I or II dislocations serve as GNDs to accommodate the strain gradient of GNT Cu, as reported in [19].

In fact, statistic results based on plenty of SEM and TEM observations show that 14% of grains in deformed GNT-100% and only 7% of grains in GTLs of GNT-50% have BCDs structures, as shown in Fig. 5f. BCDs are rarely seen in GNT-10% with 1% of gains with BCDs near the interfaces.

### 3.4. Back stress and effective stress of GNT Cu samples

The partitioning of flow stress into back stress and effective stress [22,34,39] is used to explore the strengthening kinematics of GNT Cu. Fig. 6a shows the loading-unloading-reloading (LUR) tensile curves of GNT-10% and GNT-100% and the freestanding Ⓐ and Ⓓ. All four samples exhibit the typical hysteresis loops during LUR process. A typical hysteresis loop of GNT-100% is magnified in Fig. 6b. During unloading, the curve deviates obviously from the elastic unloading and the reverse yielding happens despite that the flow stress is still tensile, indicating a pronounced Bauschinger effect with strong back stress. Accordingly, high back stress but low effective stress can be clearly detected from the Dickson method to partitioning flow stress [33].

Fig. 6c shows the back stress evolution with straining of the four samples. The back stress of the freestanding Ⓐ increases quickly to a saturated value of 344 MPa at $\varepsilon_{app}$=~2%, which contributes about 75% for its flow stress. While the back stress of freestanding Ⓓ is 118 MPa at $\varepsilon_{app}$=~2%, still contributing 60% for the flow stress. Such strong back stress in HNT Cu originates from the incompatible deformation between twin and matrix as a salient feature of nanotwinned structures. The back stresses also rapidly increase to 283 MPa (75% of flow stress) for GNT-10% and 299 MPa for GNT-100% with straining to $\varepsilon_{app}$=~2%. Both back stresses are higher than the rule-of-mixture value (231 MPa) in terms of two freestanding components.

However, the effective stress of GNT Cu is less sensitive to $f_g$, as shown in Fig. 6d. Two freestanding components were still introduced as references. The effective stresses of freestanding Ⓐ and Ⓓ increase quickly to a saturated value of 114 MPa and 81 MPa at $\varepsilon_{app}$=~2%, respectively, which are much smaller than their back stresses (Fig. 6c). Both GNT-10% and GNT-100% have similar saturated effective stresses of about ~100 MPa, comparable to the rule-of-mixture effective stress (98 MPa). The above result suggests that the extra strengthening of GNT Cu samples mainly originates from the extra back stress, rather than the effective stress.

### 3.5. Plastic strain localization and fracture behaviors of GNT Cu samples

Next, we analysis the distribution of tensile strain ($\varepsilon_x$) on the top surface (x-y plane, colored by purple in Fig. 7a) of

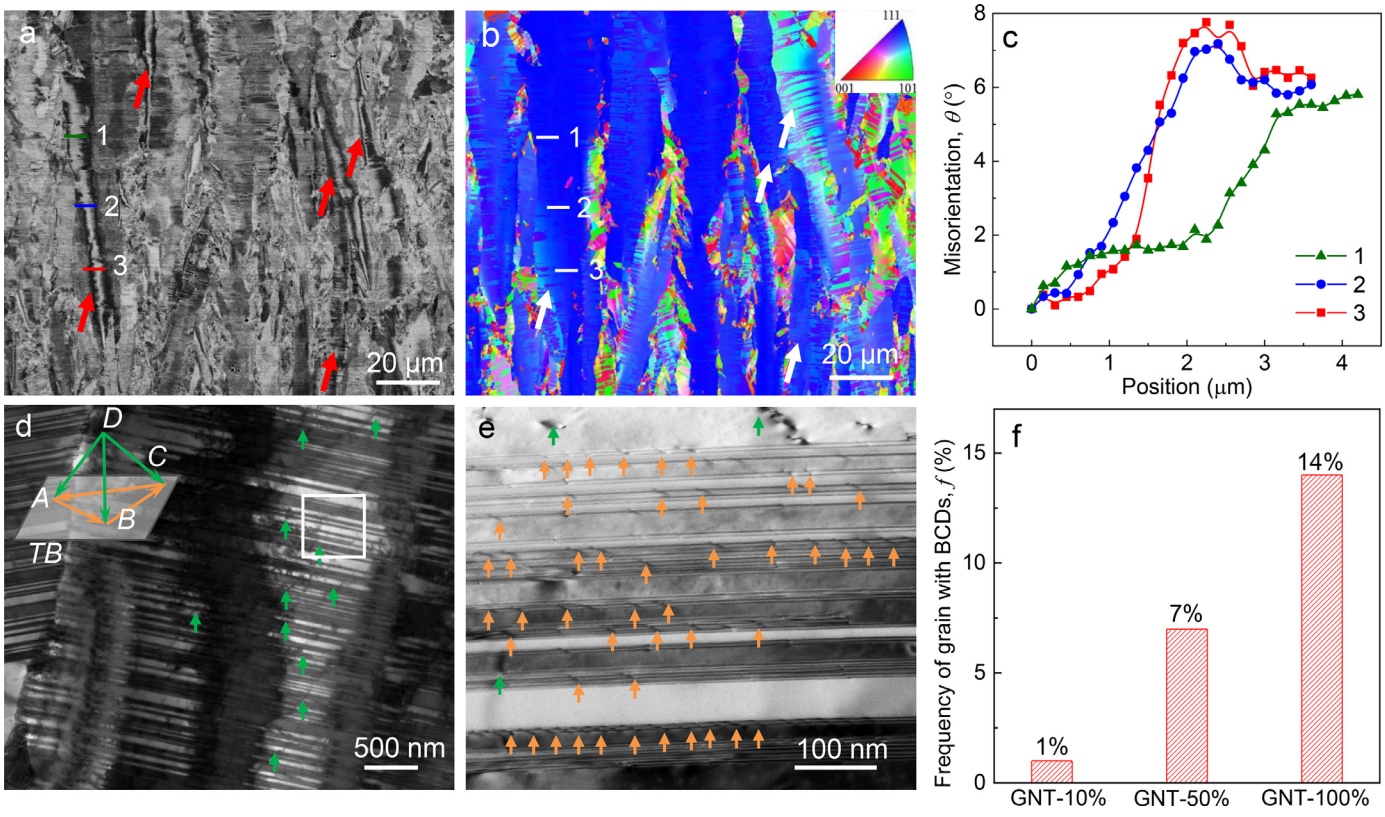


**Fig. 5.** Cross-sectional (*x-z* plane) microstructure of GNT-100% deformed at $\varepsilon_{app}$=1%. SEM image (a) and corresponding EBSD orientation mapping (b). (c) Misorientation variations along the lines labelled by 1, 2 and 3 across a BCD in (a) and (b). (d) TEM image of a BCD and (e) magnified TEM image of the white square in (d) under the diffraction vector of $g$ = 200. Mode I and mode II dislocations are indicated by green and orange arrows, respectively. (f) Frequency of grains with BCDs of three GNT samples.

GNT Cu samples. As for GNT-10%, the strain at $\varepsilon_{app}$=1% is distributed quite uniformly (Fig. 7b1); the strain localization appears at $\varepsilon_{app}$=5% (Fig. 7b2) and gets severely when $\varepsilon_{app}$ increases up to 7% (Fig. 7b3). On the contrary, no strain localization appears in GNT-100% until $\varepsilon_{app}$=5%, as shown in Fig. 7c1-c2. A weaker strain localization happens in GNT-100% at $\varepsilon_{app}$=7%, which means the larger $f_g$ helps to alleviate the strain localization.

We also compare the fracture behaviors on the top surface (x-y plane) and the cross section (*x-z* plane) of both GNT-10% and GNT-100% during tensile deformation. In GNT-10%, obvious necking with a local strain of 19% (estimated by area reduction) is observed in Fig. 8a. Fig. 8b-d show cross-sectional microstructures at ~400 $\mu$m away from the fracture surface. Micro-cracks mainly happen in Ⓐ (Fig. 8b), rather than near the interfaces (Fig. 8c), which might relate to the GND storage (Fig. 4f). Only a few micro-cracks at grain boundaries sporadically appear in Ⓓ (Fig. 8c and 8d), due to the higher work hardening capacity resulting from the larger grain size.

Compared to GNT-10%, GNT-100% has less and smaller micro-cracks even at a local strain as large as 25% (upon necking), as shown in Fig. 8f-8h. Numerous BCDs are detected in Fig. 8g and 8h, and they are helpful to suppress the formation of micro-cracks.

### 3.6. GNDs-distribution dominated strengthening mechanism

Above experimental results clarify that the volume fraction of the gradient transition layer ($f_g$) plays a significant role in the mechanical properties and deformation behaviors of GNT Cu. As $f_g$ increases, a better combination of strength and elongation achieved (Fig. 2a and Table 1). Moreover, the larger $f_g$ not only prolongs the elastic-to-plastic deformation (Fig. 2b), but also suppresses the strain localization (Fig. 7) and micro-cracks formation (Fig. 8) at subsequent plastic deformation. The strain gradient becomes smoother with increasing $f_g$, i.e., strain gradient localizes only near interfaces in GNT-10% but spans throughout the whole cross-section in GNT-100% (Fig. 3).

Generally, GNDs existing in the GTLs are regarded to contribute for the superior mechanical properties of HNS materials and accommodate the plastic strain gradient [3,4,8]. The density of GNDs is an important parameter of general interest in strengthening and hardening mechanics. According to the classical theory of strain gradient plasticity, the density of GNDs is estimated by its proportionality to the plastic strain gradient [23–25]. In this study, the plastic strain gradient arises from the progressive plastic yielding from soft Ⓓ to hard Ⓐ. So, the overall density of GNDs of GNT Cu is estimated as

$$\overline{\rho}_{GND}=\frac{2\Delta\sigma_y}{bEt} \tag{4}$$

where $\Delta\sigma_y$ is the yield strength discrepancy between soft Ⓓ and hard Ⓐ, $b$ is magnitude of Burgers vector, $E$ is elastic modulus. The three GNT Cu samples have the same sample thickness $t$ (~400 $\mu$m). Therefore, the overall density of GND should be the same in all GNT Cu samples. However, the above experimental results (Figs. 4 and 5) clearly indicate that the distributions of GNDs in the three GNT Cu are substantially different: most GNDs are accumulated in the narrow interface zones in GNT-10% (Fig. 4), but are widely scattered into the whole cross-section in GNT-100% (Fig. 5). Therefore, in addition to the density of GNDs, the influence of the distribution of GNDs in strengthening behaviors cannot be ignored but deserves further consideration.

The strengthening mechanisms related to dislocations can be understood in terms of isotropic and kinematic hardening, which

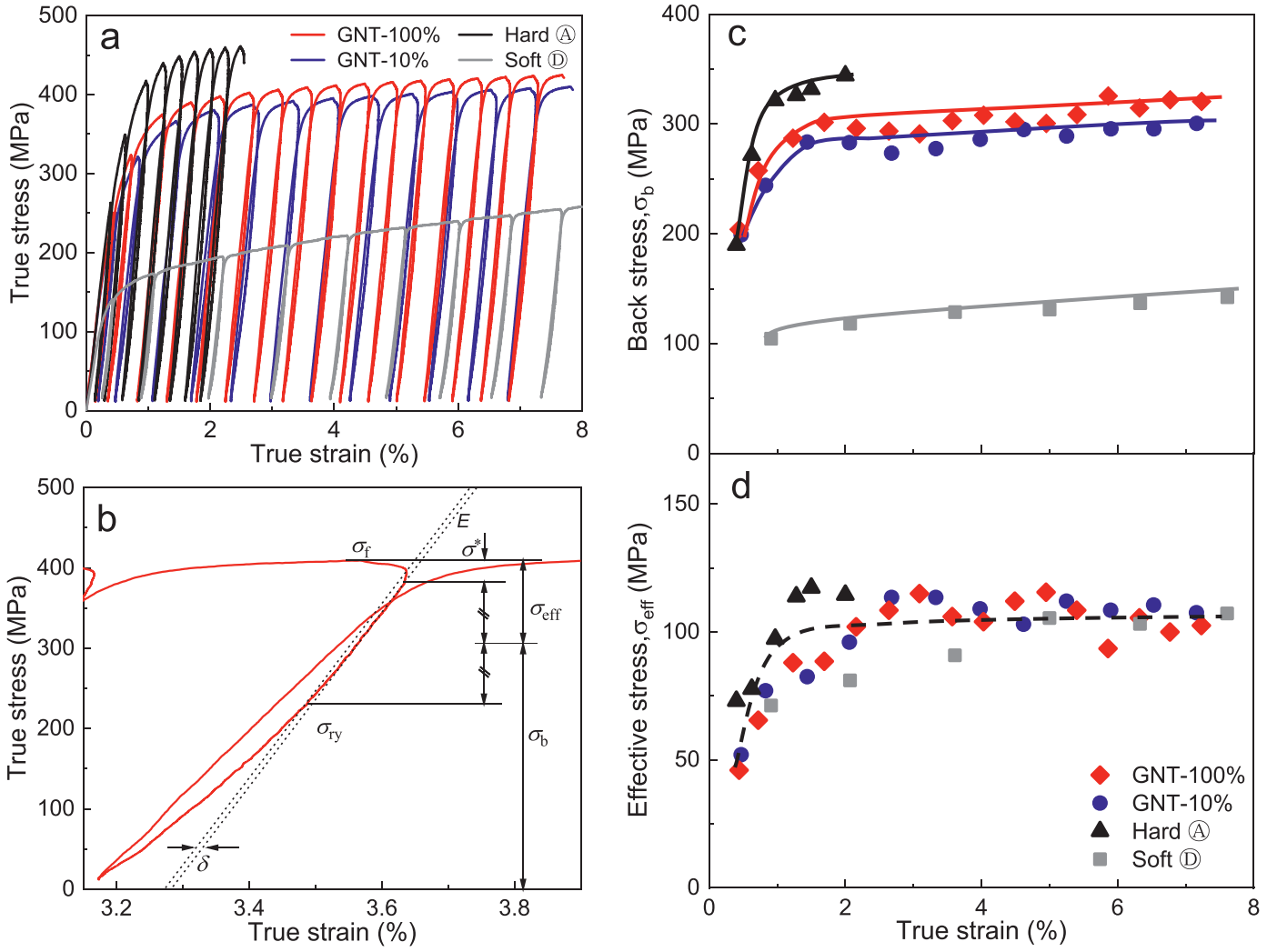


**Fig. 6.** (a) Loading-unloading-reloading true stress-strain curves for GNT-10% and GNT-100% and their freestanding Ⓐ and Ⓓ components. (b) Definition of back stress $\sigma_b$ and effective stress $\sigma_{eff}$ at the unloading curve based on Dickson's method in a magnified unloading-reloading loop of GNT-100% sample. $\sigma_f$, flow stress; $\sigma_{ry}$, reverse yield stress; $\sigma^*$, the stress interval past the peak stress; $\delta$, offset strain; $E$, elastic modulus. The variation of back stress (c) and effective stress (d) with true strains of GNT-10%, GNT-100%, Ⓐ and Ⓓ components.

correspond to effective stress and back stress, respectively, after partitioning the flow stress [27,34,39,40]. The isotropic hardening stems mainly from the random short-range interactions of dislocations with each other and also is called by forest hardening or Taylor strengthening [34,36]. which is depicted by the well-known Taylor formula [41],

$$\sigma = \alpha M \mu b \sqrt{\rho} \tag{5}$$

where $M$ is Taylor coefficient, $\mu$ is shear modulus, $\rho$ is dislocation density and $\alpha$ is a geometrical factor related to the arrangement of the dislocation pattern as discussed above. From this, the Taylor strengthening depends not only on the dislocation density but also on its distribution [42–44]. As dislocation density keeps constant, Taylor strengthening is significantly reduced as dislocation pattern varies from random dislocations to dislocation walls. The intrinsic mechanism is related to the less effective cut-off among dislocations in the presence of many immobile dislocation walls [42]. Besides the statistically stored dislocations for sustaining plastic deformations, GNDs accommodating plastic strain gradient also contribute to the effective stress $\sigma_{eff}$, as estimated in the developed Taylor formula by Mughrabi [43]:

$$\sigma_{eff} = \alpha M \mu b \sqrt{\rho_{SSD} + \beta \rho_{GND}} \tag{6}$$

where $\rho_{SSD}$ and $\rho_{GND}$ are densities of statistically stored dislocations and GNDs, respectively. $\beta$ is another coefficient related to GND distribution, in the general case that not all GNDs but only these GNDs that are cut by glide dislocations can produce forest-dislocation hardening or contribute for the effective stress [43].

Here in present study, all GNT Cu and their freestanding components exhibit a comparable effective stress (~100 MPa), independent on the additional contribution of GNDs. This is because these GNDs are concentrated at interfaces or within BCDs in GNT Cu samples and have less opportunity to cut off glide dislocations, resulting in a small $\beta$. As a result, the effective stresses is less affected by $f_g$ but constant for GNT-10% to GNT-100%.

We further focused on the effect of GNDs distribution on kinematic hardening or back stress originating from its non-zero net Burgers vector [28,45,46]. Unlike the effective stress, back stress is regarded as a long-range stress filed in which the stress decreases with the distance away from GNDs [45,47]. In other words, back stress induced by GNDs exists spatially where the slip dislocations are effectively resisted, whereas the back stress might hardly affect glide dislocations far away from GNDs.

Regarding GNT-10%, GNDs are concentrated at interfaces and only mobile dislocations in or near the interface affected zone can be effectively affected by the long-range back stress. How-

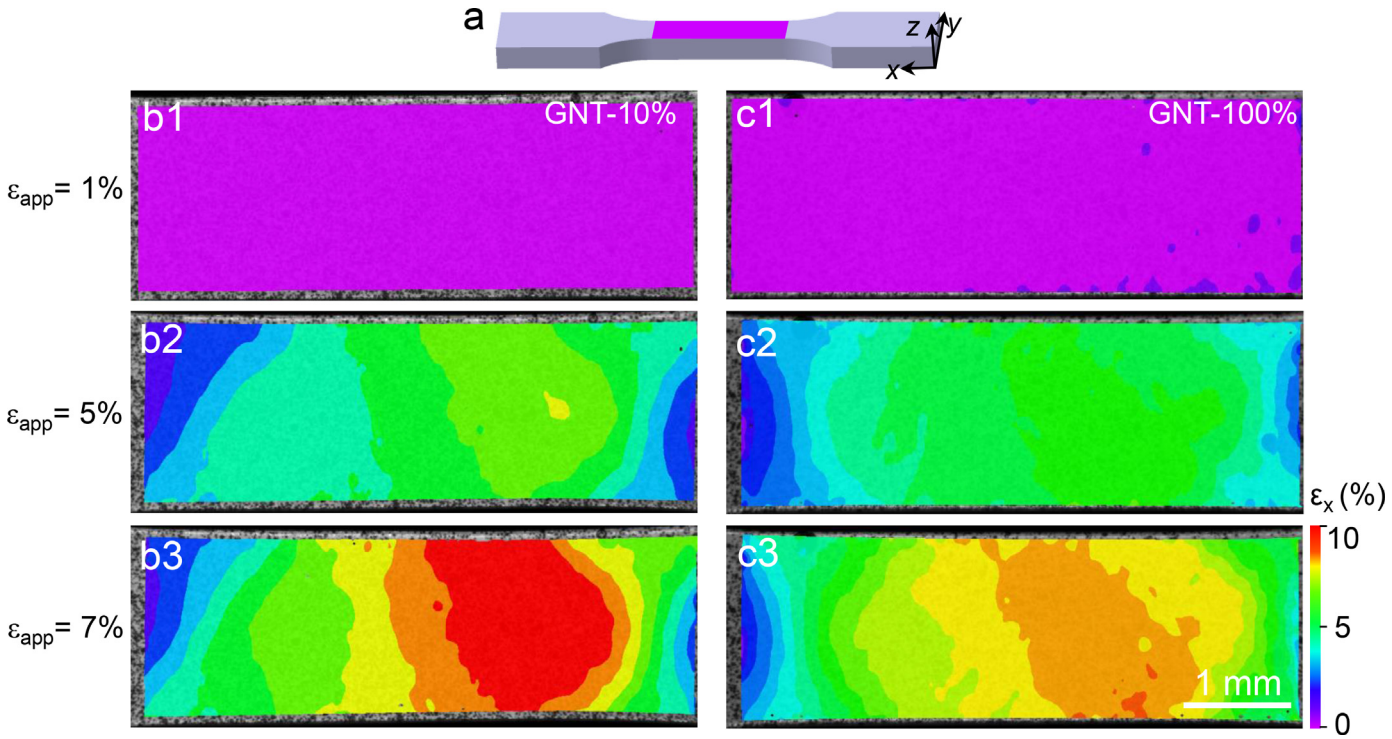


**Fig. 7.** (a) The schematics illustrating the strain distribution measurement on the top surface (*x*-*y* plane) indicated by purple in GNT Cu. The distribution of tensile strain, $\varepsilon_x$, on the surface of GNT-10% (b1-b3) and GNT-100% (c1-c3) at increasing applied tensile strain $\varepsilon_{app}$ as indicated.

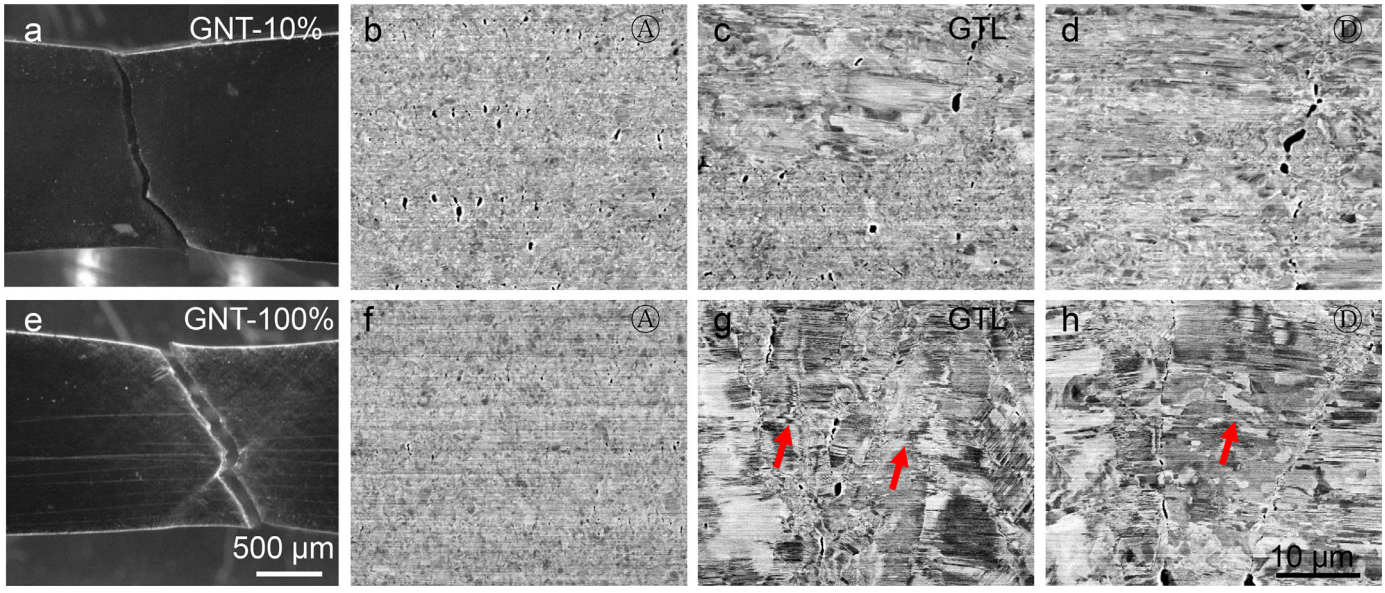


**Fig. 8.** Fracture behaviors of GNT-10% and GNT-100%. (a) Surface (*x*-*y* plane) morphologies of fracture of GNT-10%. Cross-sectional (*x*-*z* plane) microstructures of hard Ⓐ (b), GTL (c) and soft Ⓓ (d) at ~400 $\mu$m away from the fracture in GNT-10%. (e-h) are same as (a-d) except for GNT-100%. Some BCDs are indicated by red arrows.

ever, GNDs distribute widely in BCDs throughout the entire cross-section of GNT-100%. Accordingly, more mobile dislocations in larger space are effectively resisted by GNDs. In addition, from the classic plie-up model of GNDs proposed by *Bréchet* et al. [45], when GNDs are severely localized in grain boundaries in conventional polycrystalline metals, the back stress field will be screened by each other and thus the total resistance from GNDs is reduced significantly. The screening effect becomes weaker in GNT-100% due to relatively scattered BCDs serving as GND configurations compared to GNT-10%. As a result, more widely distributed GNDs produce a higher overall back stress in GNT-100%. Such, in addition to increasing the GND density, adjusting the GND distribution widely also is a feasible mechanism to improve the extra back stress or extra strengthening of GNT Cu.

### 3.7. Strain gradient plasticity model based on GND distribution

A strain gradient plasticity model has been developed to reveal the intrinsic relationship between the extra strength and structural gradient, in which the extra back stress induced by gradient structure is supposed to be proportional to GND density [19]. Here, we further modify the strain gradient plasticity model by considering

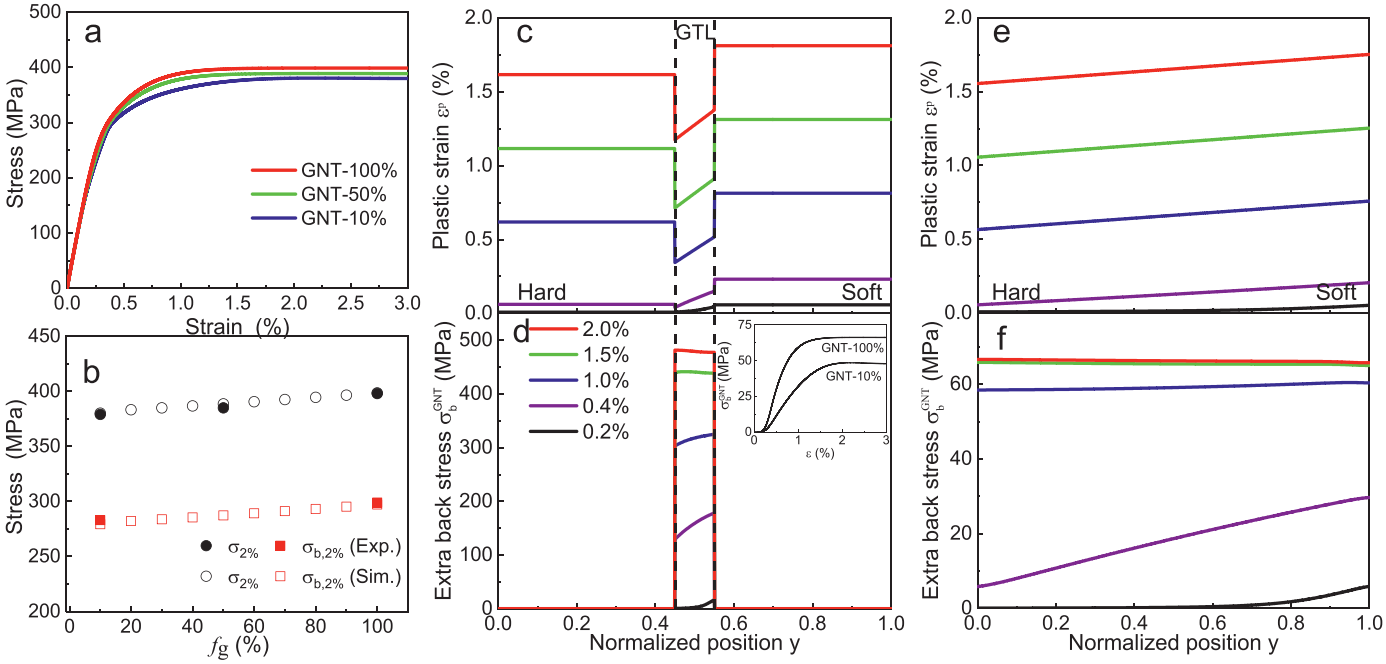


**Fig. 9.** Tensile responses of GNT Cu samples from the strain gradient plasticity modeling. (a) The stress-strain curves for GNT-10%, GNT-50% and GNT-100%. (b) The variation of tensile stress and total back stress at $\varepsilon_{app}$=2% with different $f_g$ in comparison to experimental results. The distributions of plastic strain and extra back stress across sample section for GNT-10% (c, d) and GNT-100% (e, f) at increasing applied strains as indicated. The inset in (d) shows the average extra back stress versus uniaxial tensile strain for GNT-10% and GNT-100%.

the contribution of GND distribution in addition to GND density to unravel the strengthening kinematics associated with different $f_g$. The expression can be described as follows [19,48]:

$$\sigma_b^{GNT} = \eta \mu b \rho_{GND} \tag{7}$$

where the extra back stress $\sigma_b^{GNT}$ are simultaneously determined by $\eta$ (related to GND distribution) but also $\rho_{GND}$(GND density). $\eta$ corresponds to the characteristic length where long-range back stress from GNDs can affect as proposed in [19]. According to the above discussion, $\eta$ is larger as GNDs are more widely dispersed. For simplicity, it is assumed that $\eta$ linearly relates to $f_g$ after fitting model predictions to experimental results.

Fig. 9a shows the overall stress-strain responses for GNT Cu samples with $f_g$ = 10%, 50% and 100% from the strain gradient plasticity modeling. It is clearly seen that as $f_g$ increases, the strength substantially increases especially at small strains. Fig. 9b shows the tensile stress and total back stress at $\varepsilon_{app}$=2% from strain gradient plasticity modeling. The modeling results of tensile stress as well as the total back stress of GNT Cu match well with the experimental (Figs. 2 and 6) and both show the extra strengthening of GNT samples stems from the improvement of extra back stress.

Fig. 9c shows the evolution of gradient plastic strains with straining in GNT-10%. The plastic strain happens firstly in soft component at $\varepsilon_{app}$=0.2% while the hard component still keeps elastic, resulting in plastic strain gradient in GTL. With strains up to $\varepsilon_{app}$=0.4%, the plastic strain appears across all components, i.e., the progressive yielding from soft to hard components is completed. As the applied strain increases further, the magnitude of plastic strain becomes much higher with increasing applied strains. Correspondingly, the plastic strain gradient (the slope of plastic strain along depth) also increases. Consistent with therein gradient plastic strains, the extra back stress is produced inside the GTL after $\varepsilon_{app}$=0.2% and increases quickly to a saturated value with strains up to $\varepsilon_{app}$=2% (Fig. 9d). As a result, the overall extra back stress of GNT-10% reaches quickly saturated at small strains, as shown in the inset in Fig. 9d. That means, the extra strengthening mainly happens at initial deformation stage, which agrees with the improved yield strength and prolonged elastic-to-plastic stage as found in the experimental (Figs. 2 and 9a). Notably, since the gradient deformation is supposed to happen mainly inside GTLs in the strain gradient plasticity modeling, the extra back stress improves the strength of GTL, and therefore results in a smaller plastic strain than that in either soft or hard component (Fig. 9c).

A more broadly distributed gradient plastic strains are found throughout the GNT-100% sample. As shown in Fig. 9e, the plastic strain emerges in the soft component first and gradually expands to hard component. The plastic strain exhibits a non-linear distribution at $\varepsilon_{app}$=0.2% and rapidly becomes linearly distributed at larger strains (0.4%) when all components yield, in the same way as the trend of hardness or strength (Fig. 1c3).

The extra back stress of GNT-100% produces firstly at soft components from Fig. 9f. With straining, the extra back stress becomes almost the same along the depth and quickly reaches a saturated value before $\varepsilon_{app}$=2%. Here the overall extra back stress of GNT-100% is much higher than that of GNT-10% (the inset in Fig. 9d) despite the latter has a higher local extra back stress confined at thinner GTL. The GNDs-distribution dominated strengthening behaviors based on the strain gradient plasticity model are consistent with the experimental results. All results suggest the larger $f_g$ causes the broader distribution of the plastic strain gradient (and GNDs) and the resultant extra back stress contributes to the higher overall flow stress.

The GNT Cu samples with increasing $f_g$ can be taken as prototypes to quantitatively compare the strengthening effects of heterogeneous microstructures, such as the laminated [8], partial- [3,14] and full-gradient [4] structures. These different HNS metals exhibit distinct mechanical properties, which depend on $f_g$ in the case of the constant structural gradient. A superior combination of strength and ductility is achieved in the full gradient GNT-100%. Such significant findings coincide with recent advances in fruitful full-gradient HNS materials prepared by electrodeposition [4], torsion [49,50] and laser additive manufacturing [51]. The strengthen-

ing mechanism in full-gradient microstructures originates from the stronger kinematic hardening by more scattered GNDs generated in the initial elastic-to-plastic deformation stage. Moreover, these scattered GNDs alleviate the micro-cracks (dislocation pile-ups) at grain boundaries and suppress the strain localization (Fig. 8) in the subsequent plastic deformation stage, resulting in the larger elongation in GNT-100%. In addition, the detailed interaction of scattered GNDs and statistically stored dislocations in the interiors of grains and the effect of GND distribution on statistically stored dislocations, despite which are pivotal issues beyond this study, is worthy of deep investigation in the further work. Such GND-distribution dominated strengthening mechanism shall be a significant supplementary for the classic strain gradient plasticity theory [7,23-25, 29], which has been built based on plastic strain gradient or GND density, as a guide for tailoring the high-performance HNS materials.

## 4. Conclusion

By combining experimental characterizations with modified strain gradient plasticity modeling, this study represents an improvement in mechanical properties by tuning GND distributions via quantitatively designing and controlling the volume fractions of gradient transition layer of HNS materials. With increasing $f_g$, the yield strength of GNT Cu samples can be improved without loss of uniform elongation. The strengthening mechanism originates from the more broadly-distributed strain gradient and resultant increasingly scattered distribution of GNDs as $f_g$ become larger. These scattered GNDs prefer to be accumulated into BCDs and produce higher back stress, contributing for the improved yield strength and the prolonged elastic-to-plastic stage in the initial deformation. In addition, more scattered GNDs by larger $f_g$ can suppress the strain localization and micro-crack initiation in the subsequent plastic deformation, and therefore offer the larger elongation for GNT Cu. Such GND distribution dominated strengthening mechanism not only provides a guide to optimize HNS metals but also advances the theory of strain gradient plasticity.

## Declaration of Competing Interest

The authors declare that they have no known competing financial interests or personal relationships that could have appeared to influence the work reported in this paper.

## Acknowledgement

L.L. acknowledge financial support from the National Natural Science Foundation of China (NSFC, Grant Number. 51931010, 92163202), and the Key Research Program of Frontier Science and International partnership program (GJHZ2029), Z.C. acknowledges financial support from National Natural Science Foundation of China (NSFC, Grant Number. 52001312), China Postdoctoral Science Foundation (Grant Number. BX20190336 and 2019M661150) and the IMR Innovation Fund (grant no. 2021-PY02).

## References

[1] X. Li, L. Lu, J. Li, X. Zhang, H. Gao, Mechanical properties and deformation mechanisms of gradient nanostructured metals and alloys, Nat. Rev. Mater. 5 (2020) 706–723.
[2] Y. Zhu, K. Ameyama, P.M. Anderson, I.J. Beyerlein, H. Gao, H.S. Kim, E. Lavernia, S. Mathaudhu, H. Mughrabi, R.O. Ritchie, N. Tsuji, X. Zhang, X. Wu, Heterostructured materials: superior properties from hetero-zone interaction, Mater. Res. Lett. 9 (1) (2020) 1–31.
[3] X. Wu, P. Jiang, L. Chen, F. Yuan, Y.T. Zhu, Extraordinary strain hardening by gradient structure, Proc. Natl. Acad. Sci. U. S. A. 111 (20) (2014) 7197–7201.
[4] Z. Cheng, H.F. Zhou, Q.H. Lu, H.J. Gao, L. Lu, Extra strengthening and work hardening in gradient nanotwinned metals, Science 362 (6414) (2018) 559 –+.
[5] L. Zhu, H. Ruan, A. Chen, X. Guo, J. Lu, Microstructures-based constitutive analysis for mechanical properties of gradient-nanostructured 304 stainless steels, Acta Mater. 128 (2017) 375–390.
[6] J. Li, G.J. Weng, S. Chen, X. Wu, On strain hardening mechanism in gradient nanostructures, Int. J. Plast. 88 (2017) 89–107.
[7] Y. Zhang, Z. Cheng, L. Lu, T. Zhu, Strain gradient plasticity in gradient structured metals, J. Mech. Phys. Solids 140 (2020).
[8] C.X. Huang, Y.F. Wang, X.L. Ma, S. Yin, H.W. Höppel, M. Göken, X.L. Wu, H.J. Gao, Y.T. Zhu, Interface affected zone for optimal strength and ductility in heterogeneous laminate, Mater. Today 21 (7) (2018) 713–791.
[9] M. Göken, H.W. Höppel, Tailoring nanostructured, graded, and particle-reinforced Al laminates by accumulative roll bonding, Adv. Mater. 23 (22–23) (2011) 2663–2668.
[10] M.-Y. Seok, J.-A. Lee, D.-H. Lee, U. Ramamurty, S. Nambu, T. Koseki, J.-I. Jang, Decoupling the contributions of constituent layers to the strength and ductility of a multi-layered steel, Acta Mater. 121 (2016) 164–172.
[11] J. Wang, Q. Zhou, S. Shao, A. Misra, Strength and plasticity of nanolaminated materials, Mater. Res. Lett. 5 (1) (2016) 1–19.
[12] J.G. Kim, S.M. Baek, H.H. Lee, K.-G. Chin, S. Lee, H.S. Kim, Suppressed deformation instability in the twinning-induced plasticity steel-cored three-layer steel sheet, Acta Mater. 147 (2018) 304–312.
[13] X. Ma, C. Huang, J. Moering, M. Ruppert, H.W. Höppel, M. Göken, J. Narayan, Y. Zhu, Mechanical properties of copper/bronze laminates: role of interfaces, Acta Mater. 116 (2016) 43–52.
[14] T.H. Fang, W.L. Li, N.R. Tao, K. Lu, Revealing extraordinary intrinsic tensile plasticity in gradient nano-grained copper, Science 331 (6024) (2011) 1587–1590.
[15] T. Roland, D. Retraint, K. Lu, J. Lu, Fatigue life improvement through surface nanostructuring of stainless steel by means of surface mechanical attrition treatment, Scr. Mater. 54 (11) (2006) 1949–1954.
[16] Y. Lin, J. Pan, H.F. Zhou, H.J. Gao, Y. Li, Mechanical properties and optimal grain size distribution profile of gradient grained nickel, Acta Mater. 153 (2018) 279–289.
[17] S.Q. Deng, A. Godfrey, W. Liu, N. Hansen, A gradient nanostructure generated in pure copper by platen friction sliding deformation, Scr. Mater. 117 (2016) 41–45.
[18] Z. Cheng, L. Lu, The effect of gradient order on mechanical behaviors of gradient nanotwinned Cu, Scr. Mater. 164 (2019) 130–134.
[19] Z. Cheng, L. Bu, Y. Zhang, H. Wu, T. Zhu, H. Gao, L. Lu, Unraveling the origin of extra strengthening in gradient nanotwinned metals, Proc. Natl. Acad. Sci. U. S. A. 119 (3) (2022).
[20] J. Li, S. Chen, X. Wu, A.K. Soh, A physical model revealing strong strain hardening in nano-grained metals induced by grain size gradient structure, Mater. Sci. Eng. A 620 (2015) 16–21.
[21] Z. Zeng, X. Li, D. Xu, L. Lu, H. Gao, T. Zhu, Gradient plasticity in gradient nano–grained metals, Extreme Mech. Lett. 8 (2016) 213–219.
[22] Y. Zhu, X. Wu, Perspective on hetero-deformation induced (HDI) hardening and back stress, Mater. Res. Lett. 7 (10) (2019) 393–398.
[23] M.F. Ashby, The deformation of plastically non-homogeneous materials, Philos. Mag. 21 (170) (1970) 399–424.
[24] N.A. Fleck, G.M. Muller, M.F. Ashby, J.W. Hutchinson, Strain gradient plasticity: theory and experiment, Acta Metall. Mater. 42 (2) (1994) 475–7487.
[25] H. Gao, Y. Huang, W.D. Nix, J.W. Hutchinson, Mechanism based strain gradient plasticity-I. Theory, J. Mech. Phys. Solids 47 (6) (1999) 1239–1263.
[26] L.P. Kubin, A. Mortensen, Geometrically necessary dislocations and strain-gradient plasticity: a few critical issues, Scr. Mater. 48 (2002) 119–125.
[27] N.A. Fleck, M.F. Ashby, J.W. Hutchinson, The role of geometrically necessary dislocations in giving material strengthening, Scr. Mater. 48 (2) (2003) 179–183.
[28] C.J. Bayley, W.A.M. Brekelmans, M.G.D. Geers, A comparison of dislocation induced back stress formulations in strain gradient crystal plasticity, Int. J. Solids Struct. 43 (24) (2006) 7268–7286.
[29] L. Bardella, A deformation theory of strain gradient crystal plasticity that accounts for geometrically necessary dislocations, J. Mech. Phys. Solids 54 (1) (2006) 128–160.
[30] H. Mughrabi, Dual role of deformation-induced geometrically necessary dislocations with respect to lattice plane misorientations and/or long-range internal stresses, Acta Mater. 54 (13) (2006) 3417–3427.
[31] W.D. Nix, H. Gao, Indentation size effects in crystalline materials: a law for strain gradient plasticity, J. Mech. Phys. Solids 46 (3) (1998) 411.
[32] H. Wang, Z. You, L. Lu, Kinematic and isotropic strain hardening in copper with highly aligned nanoscale twins, Mater. Res. Lett. 6 (6) (2018) 333–338.
[33] J.I. Dickson, J. Boutin, L. Handfield, A comparison of two simple methods for measuring cyclic internal and effective stresses, Mater. Sci. Eng. A 64 (1984) L7–L11.
[34] X. Feaugas, On the origin of the tensile flow stress in the stainless steel AISI 316L at 300 K: back stress and effective stress, Acta Mater. 47 (13) (1999) 3617–3632.
[35] T. Wan, Z. Cheng, L. Bu, L. Lu, Work hardening discrepancy designing to strengthening gradient nanotwinned Cu, Scr. Mater. 201 (2021).
[36] U.F. Kocks, H. Mecking, Physics and phenomenology of strain hardening: the FCC case, Prog. Mater. Sci. 48 (3) (2003) 171–273.
[37] C.W. Bert, E.J. Mills, W.S. Hyler, Effect of variation in Poisson's ratio on plastic tensile instability, J. Basic Eng. 89 (1) (1967) 35–39.
[38] Q. Lu, Z. You, X. Huang, N. Hansen, L. Lu, Dependence of dislocation structure on orientation and slip systems in highly oriented nanotwinned Cu, Acta Mater. 127 (2017) 85–97.

[39] S. Allain, O. Bouaziz, A quantitative modeling of the unloading behavior of metals during a tensile test, Int. J. Mat. Res. 101 (12) (2010) 1497–1502.
[40] M. Yang, Y. Pan, F. Yuan, Y. Zhu, X. Wu, Back stress strengthening and strain hardening in gradient structure, Mater. Res. Lett. 4 (3) (2016) 145–151.
[41] G.I. Taylor, The mechanism of plastic deformation of crystals. Part I.—Theoretical, Proc. R. Soc. London, Ser. A 145 (1934) 362–387.
[42] H. Mughrabi, A two-parameter description of heterogeneous dislocation distributions in deformed metal crystals, Mater. Sci. Eng. A 85 (1987) 15–31.
[43] H. Mughrabi, The $\alpha$ -factor in the Taylor flow-stress law in monotonic, cyclic and quasi-stationary deformations: dependence on slip mode, dislocation arrangement and density, Curr. Opin. Solid State Mater. Sci. 20 (6) (2016) 411–420.
[44] T. Ungár, A.D. Stoica, G. Tichy, X.-L. Wang, Orientation-dependent evolution of the dislocation density in grain populations with different crystallographic orientations relative to the tensile axis in a polycrystalline aggregate of stainless steel, Acta Mater. 66 (2014) 251–261.
[45] C.W. Sinclair, W.J. Poole, Y. Bréchet, A model for the grain size dependent work hardening of copper, Scr. Mater. 55 (8) (2006) 739–742.
[46] H. Mughrabi, Deformation-induced long-range internal stresses and lattice plane misorientations and the role of geometrically necessary dislocations, Philos. Mag. 86 (25–26) (2006) 4037–4054.
[47] R. Kositski, D. Mordehai, Role of dislocation pile-ups in nucleation-controlled size-dependent strength of Fe nanowires, Acta Mater. 136 (2017) 190–201.
[48] Y. Zhang, K. Ding, Y. Gu, W. Chen, Y.M. Wang, J. El-Awady, D.L. McDowell, T. Zhu, Modeling of microscale internal stresses in additively manufactured stainless steel, Modell. Simul. Mater. Sci. Eng. 30 (7) (2022).
[49] Q. Pan, L. Zhang, R. Feng, Q. Lu, K. An, A.C. Chuang, J.D. Poplawsky, P.K. Liaw, L. Lu, Gradient cell–structured high-entropy alloy with exceptional strength and ductility, Science 374 (2021) 984–989.
[50] Y. Wei, Y. Li, L. Zhu, Y. Liu, X. Lei, G. Wang, Y. Wu, Z. Mi, J. Liu, H. Wang, H. Gao, Evading the strength-ductility trade-off dilemma in steel through gradient hierarchical nanotwins, Nat. Commun. 5 (2014) 3580.
[51] R. Li, Y. Wang, N. Xu, Z. Yan, S. Li, M. Zhang, J. Almer, Y. Ren, Y.-D. Wang, Unveiling the origins of work-hardening enhancement and mechanical instability in laser shock peened titanium, Acta Mater. 229 (2022).